Estimation of Hydraulic Properties of a Sandy Soil Using Ground-Based Active and Passive Microwave Remote Sensing

François Jonard, Lutz Weihermüller, Mike Schwank, Khan Zaib Jadoon, Harry Vereecken, and Sébastien Lambot

***Abstract*—In this paper, we experimentally analyzed the feasibility of estimating soil hydraulic properties from 1.4 GHz radiometer and 0.8–2.6 GHz ground-penetrating radar (GPR) data. Radiometer and GPR measurements were performed above a sand box, which was subjected to a series of vertical water content profiles in hydrostatic equilibrium with a water table located at different depths. A coherent radiative transfer model was used to simulate brightness temperatures measured with the radiometer. GPR data were modeled using full-wave layered medium Green's functions and an intrinsic antenna representation. These forward models were inverted to optimally match the corresponding passive and active microwave data. This allowed us to reconstruct the water content profiles, and thereby estimate the sand water retention curve described using the van Genuchten model. Uncertainty of the estimated hydraulic parameters was quantified using the Bayesian-based DREAM algorithm. For both radiometer and GPR methods, the results were in close agreement with *in situ* time-domain reflectometry (TDR) estimates. Compared with radiometer and TDR, much smaller confidence intervals were obtained for GPR, which was attributed to its relatively large bandwidth of operation, including frequencies smaller than 1.4 GHz. These results offer valuable insights into future potential and emerging challenges in the development of joint analyses of passive and active remote sensing data to retrieve effective soil hydraulic properties.**

***Index Terms*—Bayesian uncertainty, ground-penetrating radar (GPR), inverse modeling, microwave radiometry, soil hydraulic properties.**

I. INTRODUCTION

HYDROLOGICAL states of the terrestrial land surface affect energy and mass fluxes between the atmosphere and the land surface [1], [2]. Accurate knowledge of these transfer processes is very relevant to improve predictions of weather, environmental disasters, food production, and in general, to advance research on climate change and adaptation. Surface energy and water fluxes are estimated from land surface models, which depend on forcing data (e.g., atmospheric data) and a wide range of parameters, including radiative, vegetation, and soil parameters. In particular, soil hydraulic properties are crucial for accurate modeling of water fluxes in soils.

Typically, estimates of soil hydraulic properties rely either on laboratory measurements based on undisturbed soil samples [3], [4] or they are based on soil water content data normally extracted from soil samples, *in situ* time-domain reflectometry (TDR) [5] or tensiometry. However, given the inherent spatial variability of soil hydraulic properties, these measurements are usually not very representative and fail to describe large-scale hydrological processes [6], [7]. For field- to catchment-scale applications, pedotransfer functions are typically used to estimate soil hydraulic properties from more easily measurable soil properties (i.e., soil texture, bulk density, organic matter content, water content, etc.) [8], [9]. However, these functions suffer from relatively large uncertainties due to the lack of detailed soil maps and the heterogeneous nature of soils [10], [11].

Remote sensing techniques offer a possible solution, as much larger areas can be observed compared with *in situ* measurements. Since the 1980s, microwave remote sensing has been increasingly used to provide hydrologically relevant data at large scales [12]–[19]. Remote measurements at microwave frequencies are sensitive with respect to the amount of liquid soil water. This makes both passive and active remote sensors very attractive for deriving information on hydrological states (e.g., soil moisture), and likewise on soil hydraulic properties. As the dependence of the microwave measurement on soil moisture is highest in the low-microwave region (< 10 GHz), microwave sensors operate in either the L-band (frequency $f = 1$–2 GHz, wavelength $\lambda = 30$–$15\,\mathrm{cm}$), C-band ($f = 4$–8 GHz, $\lambda = 7.5$–$3.8\,\mathrm{cm}$), or the X-band ($f = 8$–12 GHz, $\lambda = 3.8$–$2.5\,\mathrm{cm}$). In particular, remote signals in the L-band permit deeper characterization depth as a consequence of lower attenuation and scattering in natural media such as soils and vegetation. In this context, the European Space Agency (ESA) initiated the Soil Moisture and Ocean Salinity (SMOS) mission [20], [21]. Since May 2010, the L-band radiometer MIRAS on board the SMOS satellite has been measuring multiangular brightness temperatures with approximately

Manuscript received January 13, 2014; revised September 22, 2014; accepted October 31, 2014. This work was supported by the Helmholtz Alliance on "Remote Sensing and Earth System Dynamics" and by the CROPSENSe project funded by the German Federal Ministry of Education and Research (BMBF). The ELBARA-II radiometer was provided by TERENO "Terrestrial Environmental Observatories", also funded by the BMBF.

F. Jonard, L. Weihermüller, and H. Vereecken are with Agrosphere (IBG-3), Institute of Bio- and Geosciences, Forschungszentrum Jülich GmbH, 52425 Jülich, Germany (e-mail: f.jonard@fz-juelich.de; l.weihermueller@fz-juelich.de; h.vereecken@fz-juelich.de).

M. Schwank is with Swiss Federal Institute for Forest, Snow and Landscape Research (WSL), 8903 Birmensdorf, Switzerland, and also with GAMMA Remote Sensing AG, 3073 Gümligen, Switzerland (e-mail: mike@schwank.ch).

K. Z. Jadoon is with Water Desalination and Reuse Center, King Abdullah University of Science and Technology, Thuwal 23955-6900, Saudi Arabia (e-mail: Khan.Jadoon@kaust.edu.sa).

S. Lambot is with Earth and Life Institute, Université catholique de Louvain, 1348 Louvain-la-Neuve, Belgium (e-mail: sebastien.lambot@uclouvain.be).

Color versions of one or more of the figures in this paper are available online at http://ieeexplore.ieee.org.

Digital Object Identifier 10.1109/TGRS.2014.2368831

40-km spatial resolution and a global revisit time of approximately three days [22]. In addition, the National Aeronautics and Space Administration plans to launch the Soil Moisture Active Passive (SMAP) mission in 2015 [23]. The SMAP mission objective is to provide soil moisture estimates at 9-km resolution and global coverage with a revisit time of approximately three days. This product will be obtained from coinciding measurements of low-resolution L-band brightness temperature and high-resolution L-band radar backscatter. SMAP soil moisture retrieval seeks to optimally combine the complementary sensitivities of passive and active L-band signals with respect to soil moisture and vegetation/soil surface roughness and the different spatial resolutions of the sensors [24].

Although many studies have been initiated in support of the SMOS and SMAP missions, most of them have focused on the estimation of surface soil moisture, given the fact that the L-band measurements mainly depend on the water content of the first few centimeters of the soil. However, several authors have investigated the possibility of remotely retrieving soil hydraulic properties using a combination of hydrological models, radiative transfer (RT) models, and time series of remotely sensed soil moisture data [25]–[28]. Even if several of these studies were validated against reference measurements, the large heterogeneity in, e.g., soil water content, soil surface roughness, and vegetation restricted the reliable assessment of the proposed methods. Recently, Santanello *et al.* [29] have used soil moisture estimates derived from passive and active microwave remote sensing to calibrate a land surface model and to infer soil hydraulic properties. In order to obtain physically meaningful estimates of soil hydraulic properties, pedotransfer functions were used in the land surface model. Harrison *et al.* [30] extended the study of Santanello *et al.* [29] to include an estimation of uncertainty with regard to soil hydraulic properties. Researchers, such as Ines and Mohanty [31], performed synthetic studies to assess soil hydraulic parameters derived from remote sensing. Montzka *et al.* [32] used a data assimilation approach by means of which synthetic data were used to estimate soil hydraulic properties from L-band satellite data. The performance of the proposed approach was evaluated for four different soil types. However, only homogeneous soils were considered in this study. A review of recent developments related to soil hydraulic property estimation using remote sensing is given by Mohanty [33].

At the field scale, a number of geophysical methods such as electromagnetic induction, electrical resistance tomography, and ground-penetrating radar (GPR) are increasingly used to provide valuable information on the hydrological properties of the vadose zone. Field-scale techniques are particularly relevant for supporting agricultural management practices and also for improving and validating spaceborne data products. Amongst them, GPR has demonstrated good performance for high-resolution soil moisture mapping at the field scale [34]–[36]. Over the past decade, significant progress has been made in the modeling of GPR data. An advance of particular interest is the full-wave modeling approach, which permits the exploitation of all the information contained in the radar data [37]–[39]. Several authors have also investigated the application of GPR to infer soil hydraulic properties mainly using cross-hole GPR data [40]–[43]. A major difficulty with these approaches is to constrain the inverse problem in order to obtain a unique solution. A promising approach is the use of a joint hydrogeophysical inversion technique, where the geophysical and hydrodynamic models constrain each other, which allows the complexity of the optimization process to be considerably reduced. Lambot *et al.* [44] applied this method using off-ground GPR data to estimate the hydraulic properties of a laboratory sand during an infiltration event. Despite the relatively large frequency band of the radar and the laboratory-controlled conditions, some differences were observed between the inverted soil hydraulic properties and direct measurements on soil samples, which were attributed to inherent heterogeneities and different characterization scales. Recently, Jadoon *et al.* [45] have also applied the method locally to a bare agricultural field.

In this paper, we used radiometer and GPR data to retrieve the water retention curve of a sand subjected to a series of vertical water content profiles in hydrostatic equilibrium with a water table located at different depths. Measurements were performed at 1.4 GHz for the radiometer and in the range of 0.8–2.6 GHz for the GPR. Radiometer data were described using a coherent RT model, whereas GPR data were modeled using full-wave layered medium Green's functions. Radiometer and GPR forward models were inverted to estimate the sand water retention curve and the related hydraulic parameters. Uncertainty of the estimated hydraulic parameters was quantified in a Bayesian framework using the DREAM algorithm [46]. The hydraulic parameters estimated from GPR and radiometer data were compared against reference laboratory measurements and estimates from TDR. The main benefits of TDR compared with the reference laboratory characterization are: 1) the *in situ* measurements; and 2) the larger characterization scale, both making TDR more comparable with the GPR and radiometer measurements given the inherent variability in the sand. In addition, TDR being a dielectric sensor, will be affected in the same way as GPR and radiometer with respect to uncertainties in the relationship between permittivity and water content. However, TDR may suffer from bias in the permittivity estimates, which is not easily quantifiable. This study represents the first attempt to compare passive and active microwave sensing methods to remotely identify key soil hydraulic properties.

II. EXPERIMENTAL SETUP

The ground-based remote sensing experiment was conducted at the TERENO (Terrestrial Environmental Observatories) test site in Selhausen, Germany (latitude 50° 87 N, longitude 6° 45 E, 105 m above sea level). L-band radiometer and off-ground GPR measurements were performed over a wooden box (1.00-m deep and 2.00 × 2.00 m in area) filled with sand (see Fig. 1). The L-band radiometer was fixed on an aluminium arc 4 m above the ground and the antenna pointed toward the sand box with an observation angle of 36° relative to nadir. The GPR antenna was fixed above the sand box on a wooden frame (see Fig. 2). The GPR antenna aperture was situated about 0.40 m above the sand surface with normal incidence. To avoid interferences between the two instruments, the radiometer and GPR

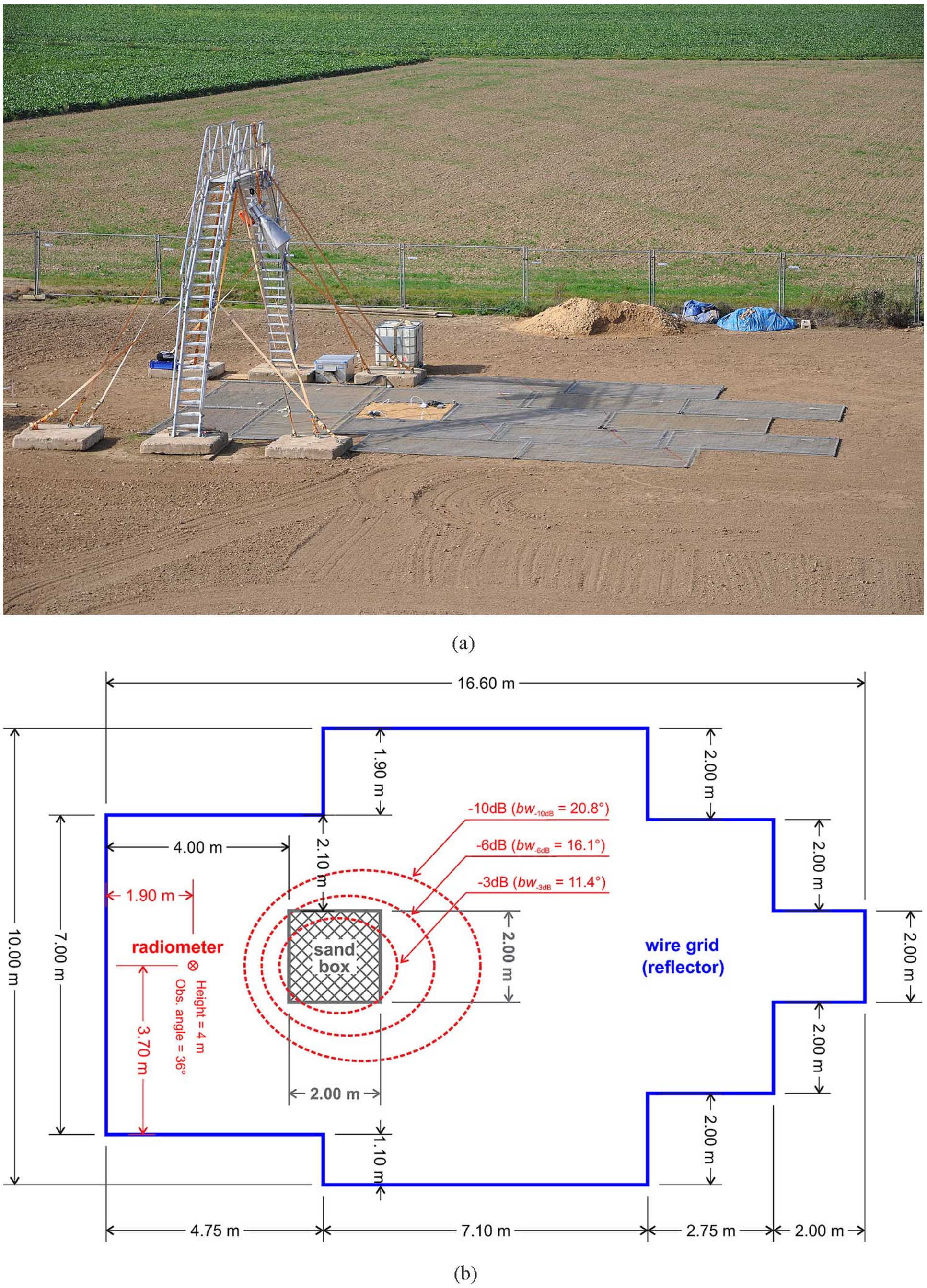

Fig. 1. (a) Picture of the experimental setup including a radiometer fixed on an arc and a sand box in the center of a wire grid at the TERENO test site in Selhausen (Germany). (b) Sketch of the experimental setup showing the location and dimensions of the sand box and the wire grid. Dashed ellipses indicate the radiometer footprints at -3, -6, and -10 dB and their respective half-beamwidth (bw) is also indicated.

measurements were not performed simultaneously. In particular, the GPR system was removed for the radiometer measurements.

The inner sides of the wooden box were covered with aluminium foil to avoid interference from the surrounding ground. Watertightness was ensured using a polyvinyl chloride foil placed against the aluminium foil. To increase the sensitivity of the radiometer measurements to radiance originating from the sand box and to minimize the influence of radiance from the surrounding area, a wire grid was placed around the sand box covering an area of approximately 122 m^2 (see Fig. 1). The mesh size of the grid was 0.5 cm, thereby emulating a perfect reflector given the $\approx$21 cm wavelength at 1.4 GHz.

Radiometer and GPR measurements were performed for seven different water table depths, ranging from the bottom of the sand box to almost the sand surface. In order to avoid increased electrical conductivity, along with increased electrical losses within the moist sand, distilled water was used to set the water table. After each change in water table depth, hydrostatic equilibrium was reached in the unsaturated zone within 6 to 11 days. This hydrostatic equilibrium caused the water content profile above the water table to follow the water retention curve of the sand. Precipitation and evaporation at the surface were prevented using a hermetic cover that was only removed for the measurements.

Fig. 2. Picture of the radar horn antenna connected to a vector network analyzer and fixed about 0.40 m above the sand surface.

A. Reference Laboratory Measurements

The soil water retention curve was determined in the laboratory by desaturating soil samples stepwise from close saturation (pressure head of -1 cm) to a pressure head of -70 cm. Therefore, soil columns with a length of 5 cm and a total volume of 100 cm^3 were filled with sand to the same bulk density as in the sand box (1.64 $\text{g} \cdot \text{cm}^{-3}$). The samples were then saturated from below by settling the samples on a sand bed with the water table adjusted to the lower end of the samples [3]. In the next step, the water table was lowered to the predefined pressure steps (-5, -10, -15, -20, -25, -30, -35, -40, -45, -50, -60, and -70 cm). For each pressure step, the water content of the column was determined by measuring the sample's weight or the cumulative water loss after hydraulic equilibrium had been reached. Equilibrium was thereby defined by a stable weight of the sample over time. To ensure reliability of the data, a minimum of six replicates were measured, whereby the measurements were also cross-checked by analyzing samples in two independent laboratories. Due to the known problems in the homogeneous vertical water content distribution of the sand sample, the applied pressure steps were corrected by adding half of the soil column length (2.5 cm) to each pressure step.

B. In Situ TDR Measurements

TDR and capacitance sensors were installed at seven different depths, i.e., 5, 10, 20, 30, 40, 60, and 80 cm, below the sand surface at two opposite sides of the sand box to measure profiles of the relative dielectric permittivity, i.e., ε, and bulk electrical conductivity, i.e., σ (see Fig. 3). TDR measurements were carried out every 20 min using homemade three-rod probes with a length of 20 cm that were inserted horizontally into the sand. TDR probes were connected to a TDR100 cable tester and a CR1000 data logger (both Campbell Scientific, Logan, Utah, USA). The TDR waveforms were analyzed using the tangent method in the time domain [47]. Bulk soil electrical conductivity and soil temperature measurements were carried out every 15 min using 5TE capacitance sensors (Decagon Devices, Inc., Pullman, Washington, USA) composed of three prongs of 5.2-cm length, also inserted horizontally into the sand. Furthermore, a piezometer was used to monitor the water table depth (see Fig. 3).

C. Remote Sensing Systems

1) L-Band Radiometer: We used the L-band radiometer ELBARA-II [48], which is the same instrument as those used by ESA for calibration and validation activities of the SMOS mission. The ELBARA-II radiometer is sensitive within the protected frequency band 1400–1427 MHz of the microwave L-band. The internal noise reference sources used to achieve calibrated brightness temperature were realized with a hot resistive noise source (at about 313 K) and an active cold source (at about 40 K). Furthermore, the noise power at the radiometer input ports was corrected for the noise added by the lossy feed cables (about 0.2 dB) assumed to be at the air temperature. A detailed description of the ELBARA-II system and of the applied calibration procedure is provided by Schwank *et al.* [48]. Each day when measurements were performed, the radiometer was calibrated by measuring sky radiance at an elevation angle of about 55° above the horizon and oriented approximately toward the north. Each radiometer measurement was performed with a 3-s integration time to achieve an absolute accuracy better than 1 K [49]. The radiometer was equipped with a dual-mode conical horn antenna $(\text{aperture diameter} = 60\,\text{cm},\ \text{length} = 67\,\text{cm})$ with symmetrical and identical beams and a -3-dB full beamwidth of 23° in the far field. The antenna directivity was derived from the time series of brightness temperatures measured with the sun passing through the antenna field of view [48].

2) Ground-Penetrating Radar: The radar measurements were carried out using an ultrawideband stepped-frequency continuous-wave radar [37], [50]. The radar system was set up using a vector network analyzer (VNA, ZVRE, Rohde & Schwarz, Munich, Germany) connected to a transmitting and receiving linear polarized double-ridged broadband horn antenna (BBHA 9120 A, Schwarzbeck Mess-Elektronik, Schönau, Germany). The antenna was connected to the reflection port of the VNA with a low-loss N-type 50-ohm impedance coaxial cable. Before each measurement, the VNA was calibrated at the connection between the coaxial cable and the antenna using a standard open-short-match calibration kit. The antenna has a length of 22 cm and a $14 \times 25\ \text{cm}^2$ aperture area. Its -3-dB full beamwidth is 26° in the E-plane and 20° in the H-plane (at 2 GHz). The antenna nominal frequency range is 0.8–5.2 GHz and its isotropic gain ranges from 4.4–14 dBi. Measurements were performed between 0.8–2.6 GHz with a frequency step of 8 MHz.

III. Modeling Approach

A. Soil Hydraulic Model

Radiometer and radar measurements were performed when the sand was in hydrostatic equilibrium with a water table located at position z_{w} [m]. In hydrostatic equilibrium, the water content profile follows the water retention curve of the soil, which we described using the van Genuchten model [51], i.e.,

$$\theta(h) = \begin{cases} \theta_{\text{r}} + (\theta_{\text{s}} - \theta_{\text{r}})\left[1 + |\alpha h|^{n}\right]^{-m} & \text{for} \quad h < 0 \\ \theta_{\text{s}} & \text{for} \quad h \geq 0 \end{cases} \tag{1}$$

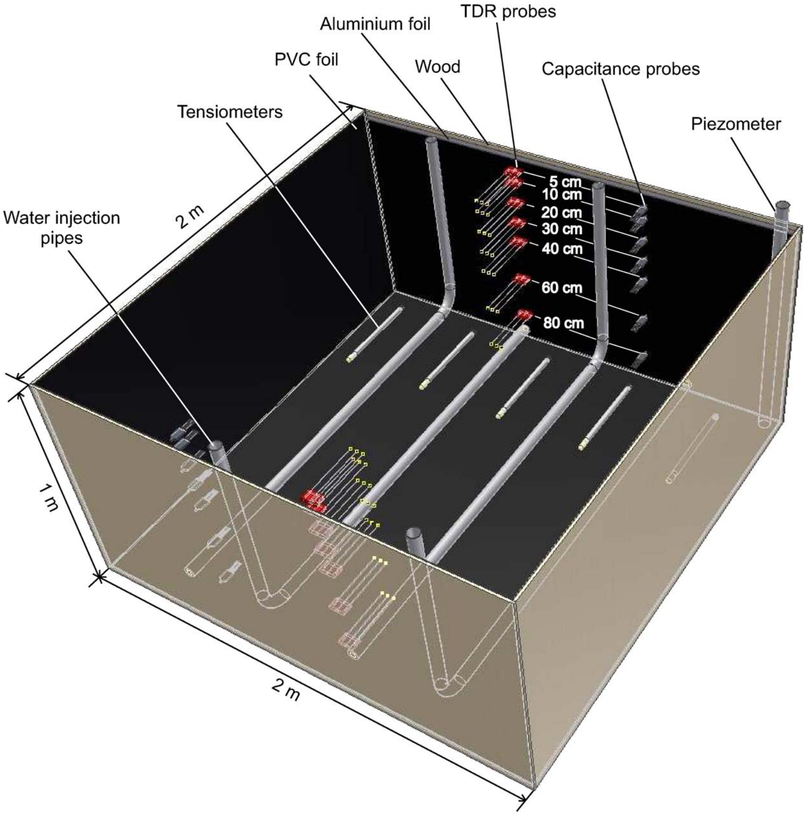

Fig. 3. Sketch of the sand box showing the location of the TDR probes, capacitance probes, tensiometers, water injection pipes, and the piezometer.

where θ [$\mathrm{m}^3 \cdot \mathrm{m}^{-3}$] is the volumetric water content, θ_r and θ_s [$\mathrm{m}^3 \cdot \mathrm{m}^{-3}$] are the residual and saturated water contents, respectively, h [m] is the pressure head, α [m^{-1}] and n [$-$] are curve shape parameters, which can be related to the inverse of the air entry value and the width of the pore size distribution, respectively, and m [$-$] is restricted by the Mualem condition as $m = 1 - 1/n$ with $n > 1$. The pressure head h is related to the vertical position z [m] by $h = z - z_\mathrm{w}$.

B. Dielectric Model

To derive the soil volumetric water content from the relative dielectric permittivity of the soil, dielectric models have been developed. Empirical models such as those introduced by Topp *et al.* [52] and Jacobsen and Schjonning [53] are often used as they do not require *a priori* information on soil properties. However, the validity range of such empirical models is limited to soils and frequencies similar to those for which these specific models were calibrated. In more physically based approaches, the soil is regarded as a mixture of different components, namely, air, soil matrix, and free water. In some cases, also bound water is considered [54]. For these models, additional information about soil properties such as the porosity and/or texture are necessary. In this paper, we used a power-law model [55], i.e.,

$$\varepsilon^\gamma = \theta\, \varepsilon_\mathrm{w}^\gamma + (\phi - \theta)\varepsilon_\mathrm{a}^\gamma + (1 - \phi)\varepsilon_\mathrm{s}^\gamma \tag{2}$$

where γ [$-$] is an empirical coefficient that depends on soil structure, ε_w, ε_a, and ε_s are the relative permittivities of water, air, and soil particles, respectively, and ϕ [$\mathrm{m}^3 \cdot \mathrm{m}^{-3}$] is the soil porosity. For this study, we used $\gamma = 0.5$, which reduces (2) to the complex refractive index model [55].

As free water dielectric losses are significant in the L-band [56], we accounted for these effects using the Debye equation [57]

$$\varepsilon_\mathrm{w} = \varepsilon_\infty + \frac{\varepsilon_\mathrm{sp} - \varepsilon_\infty}{1 - \imath\,\omega\,\tau} + \imath\,\frac{\sigma_\mathrm{DC}}{\omega\,\varepsilon_0} \tag{3}$$

where $\varepsilon_\infty = 4.9$ is the relative permittivity at infinite frequency [58], ε_sp is the static relative permittivity of pure water, $\varepsilon_0 = 8.8542 \times 10^{-12}\,\mathrm{F} \cdot \mathrm{m}^{-1}$ is the dielectric permittivity of free space, σ_DC [$\mathrm{S} \cdot \mathrm{m}^{-1}$] is the direct-current (DC) conductivity (ionic conductivity) of water, ω is the angular frequency [Hz], τ is the relaxation time [s], and $\imath = \sqrt{-1}$.

The static relative permittivity ε_sp is expressed as a function of temperature T [°C] as follows [59]:

$$\varepsilon_\mathrm{sp} = 88.045 - 0.4147\,T + 6.295 \times 10^{-4}\,T^2 + 1.075 \times 10^{-5}\,T^3. \tag{4}$$

The relaxation time τ is also temperature-dependent and is calculated as follows [60]:

$$\tau = \frac{1}{2\pi}(1.1109 \times 10^{-10} - 3.824 \times 10^{-12}T + 6.938 \times 10^{-14}T^2 - 5.096 \times 10^{-16}T^3). \tag{5}$$

C. Microwave Emission Model (Radiometer)

The first part of this section describes the model used to derive the reflectivities R_s^p of the sand box from the brightness temperatures T_B^p measured with the L-band radiometer. The subsequent part of this section outlines the approach used to relate sand box reflectivities R_s^p to water content profiles.

1) Brightness Temperatures: The thermal L-band emission, also called brightness temperature, T_B^p, is expressed with a RT model that fulfills Kirchhoff's law (e.g., [16]). To include both radiance emitted from the sand box and from the surrounding area, T_B^p at horizontal $(p = \mathrm{H})$ and vertical $(p = \mathrm{V})$ polarization is represented as a corresponding linear combination, i.e.,

$$T_\mathrm{B}^p = \eta^p \left[(1 - R_\mathrm{s}^p)\, T_\mathrm{s} + R_\mathrm{s}^p\, T_\mathrm{sky} \right] + (1 - \eta^p) \left[(1 - R_0^p)\, T_0 + R_0^p\, T_\mathrm{sky} \right]. \qquad (6)$$

The weighting factor η^p is used to express the fractional amounts of radiance emitted from the sand box (η^p) and the surrounding area covered with the wire grid $(1 - \eta^p)$.

R_s^p [−] and R_0^p [−] are the reflectivities of the sand box and the surrounding area, respectively. At thermal equilibrium, $(1 - R_\mathrm{s}^p)$ and $(1 - R_0^p)$ represent the corresponding emissivities. The downwelling sky radiance reflected at the ground is assumed to be $T_\mathrm{sky} = 4.8\,\mathrm{K}$ [61]. T_s [K] and T_0 [K] are the effective physical temperatures of the filled sand box and the surrounding area, respectively. In this paper, T_s was approximated as the arithmetic mean of the sand temperatures measured at depths of 5 and 40 cm. T_0 was approximated by the air temperature measured near the radiometer feed point.

The weighting factor η^p used in (6) is computed from the normalized antenna directivity $D(\Theta) = \exp(-0.005309\Theta^2)$ with $\Theta(x, y)$ being the polar angle between the main direction of the antenna and the position of a facet with coordinates (x, y) within the footprint plane

$$\eta = \iint_A D(\Theta(x, y))\, d\Omega(x, y, dx, dy). \qquad (7)$$

This integral is evaluated numerically over area A of the sand box, with $d\Omega(x, y, dx, dy)$ [rad] being the solid angles of footprint facets with infinitesimal areas $dxdy$. Considering all the dimensions depicted in Fig. 1(b), the evaluation of (7) yields $\eta = 0.48$. It is worth noting that η in (7) does not depend on polarization p as the antenna directivity $D(\Theta)$ can be considered as polarization independent for the symmetrical Picket horn antenna. The value of $\eta^p = 0.48$ in (6) allows us to derive the reflectivities R_0^p of the surrounding area from T_B^p measured with the sand box covered with a copper sheet acting as a reflector with $R_\mathrm{s,ref}^p = 1$. Solving (6) with $\eta^p = 0.48$ and $R_\mathrm{s,ref}^\mathrm{H} = R_\mathrm{s,ref}^\mathrm{V} = 1$ yielded $R_0^\mathrm{H} = 0.95$ and $R_0^\mathrm{V} = 0.92$.

Alternatively, the weighting factor η^p and the effective reflectivity R_0^p of the area outside the sand box are derived from (6) without *a priori* information on the antenna directivity. To this end, T_B^p was measured for two different footprint configurations: 1) the area $A = 4\,\mathrm{m}^2$ of the sand box is covered with a reflector (copper sheet); and 2) the sand box is covered with a microwave absorber (EPP22, Telemeter Elektronic, Donauwörth, Germany). The attenuation of the absorber is specified as −30 dB at the microwave L-band. Accordingly, the reflectivity of the absorber is assumed to be $R_\mathrm{s,abs}^p = 0$. Considering the T_B^p measured for the configurations (1) and (2) with associated reflectivities $R_\mathrm{s}^p = R_\mathrm{s,ref}^p = 1$ and $R_\mathrm{s}^p = R_\mathrm{s,abs}^p = 0$ in (6) yields two equations for the two unknowns η^p and R_0^p. Solving these two equations (each with $p = \mathrm{H}$ or V) for the two unknowns yielded $\eta^\mathrm{H} = \eta^\mathrm{V} = 0.54$ and $R_0^\mathrm{H} = 0.94$, $R_0^\mathrm{V} = 0.90$. Although the results derived from the two approaches were very similar, we considered the model-based values $\eta^p = 0.48$, $R_0^\mathrm{H} = 0.95$, and $R_0^\mathrm{V} = 0.92$ derived from the antenna directivity. This choice was based on the fact that the antenna directivity is considered to be more reliable than the assumption $R_\mathrm{s,abs}^p = 0$, which is crucial for the experimental approach. Finally, sand box reflectivities R_s^p can be derived from T_B^p measurements carried out for the uncovered sand box.

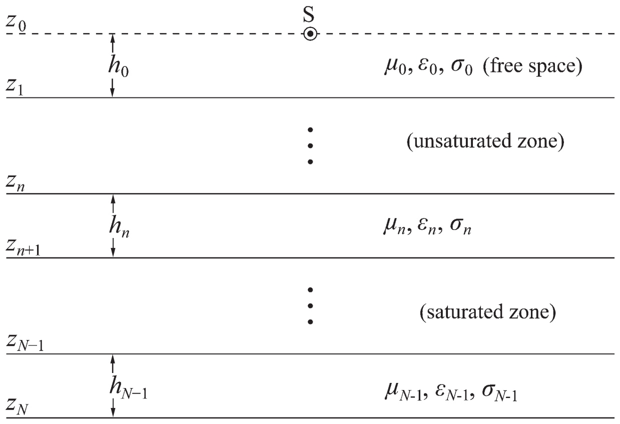

Fig. 4. Three-dimensional planar layered medium with a radar point source and receiver or a radiometer point receiver (S). Each layer is characterized by the dielectric permittivity ε_n, electric conductivity σ_n, magnetic permeability μ_n, and thickness h_n.

2) Reflectivities: Reflectivities R_s^p of the sand box can be modeled based on sand permittivity data using different approaches. A rather simple approach is to assume a constant water content along the sand depth. However, a more sophisticated approach is required to model R_s^p in order to account for the water retention curve profiles dealt with in this study. To this end, a coherent RT model [62], applicable to planar layered dielectric media, was used. This model is very efficient in terms of computation time as it uses a matrix formulation of the boundary conditions at the layer interfaces derived from Maxwell's equations. This is important in view of the fine discretization required to represent smooth dielectric profiles realistically across the sand depth. Accordingly, R_s^p were computed with the coherent RT model evaluated for N dielectric layers (distinguished by subscript $n = 1, 2, \ldots, N$) with thickness $h_n = 0.5\,\mathrm{cm}$, which corresponds to one-tenth of the minimum wavelength in the medium in order to emulate profile continuity [63]. As depicted in Fig. 4, each layer is characterized by its dielectric permittivity ε_n and its electrical conductivity σ_n. The magnetic permeability (μ_n) is considered constant and equal to the permeability of free space $(\mu_0 = 4\pi 10^{-7}\,\mathrm{H}\cdot\mathrm{m}^{-1})$. To derive the reflectivities R_s^p of the layer stack, the sand permittivity profiles and the related water content profiles were simulated using the van Genuchten model [see (1)].

D. GPR Model

The first part of this section describes the radar equation used to derive Green's functions $G_{xx}^{\uparrow}(\omega)$ from off-ground GPR measurements. Here, $G_{xx}^{\uparrow}(\omega)$ represents the backscattered electric field from the sand box normalized to a unit-strength electric source. In the second part of this section, we introduce the approach used to simulate the medium response, namely, Green's function $G_{xx}^{\uparrow}(\omega)$, based on permittivity profile information.

1) Radar Equation: The radar measurements (raw data) $S_{11}(\omega)$ can be expressed as the ratio between the backscattered electromagnetic field $b(\omega)$ and the incident electromagnetic field $a(\omega)$ at the VNA calibration plane, with ω being the angular frequency. In far-field conditions, the spatial distribution of the backscattered electromagnetic field over the antenna aperture can be assumed to be independent of the layered medium, i.e., only the phase and amplitude of the field change (homogeneous field over the antenna aperture). In this case, the following radar equation, expressed in the frequency domain, can be used to describe the radar raw data [37]

$$S_{11}(\omega) = \frac{b(\omega)}{a(\omega)} = H_{\mathrm{i}}(\omega) + \frac{H(\omega)\, G_{xx}^{\uparrow}(\omega)}{1 - H_{\mathrm{f}}(\omega)\, G_{xx}^{\uparrow}(\omega)} \tag{8}$$

where $S_{11}(\omega)$ is the international standard quantity measured by the VNA, $H_{\mathrm{i}}(\omega)$ is the global reflection coefficient of the antenna for the fields incident from the VNA calibration plane onto the point source (corresponding to the free space response of the antenna), $H(\omega) = H_{\mathrm{t}}(\omega)H_{\mathrm{r}}(\omega)$ where $H_{\mathrm{t}}(\omega)$ is the global transmission coefficient for fields incident from the VNA calibration plane onto the point source, $H_{\mathrm{r}}(\omega)$ is the global transmission coefficient for fields incident from the field point onto the VNA calibration plane, $H_{\mathrm{f}}(\omega)$ is the global reflection coefficient for the field incident from the layered medium onto the field point, and $G_{xx}^{\uparrow}(\omega)$ is the planar layered medium Green's function.

The global reflection and transmission coefficients [$H_{\mathrm{i}}(\omega)$, $H(\omega)$, and $H_{\mathrm{f}}(\omega)$] were determined by solving a system of equations [see (8)] for different model configurations. We used several well-defined configurations with the antenna at different heights above a copper plane functioning as an infinite perfect electrical conductor. Once the antenna characteristic functions are known, antenna effects can be filtered out from the radar measurements, i.e., Green's functions can be derived from the $S_{11}(\omega)$ measurements.

2) Green's Functions: The radar model used to simulate Green's functions $G_{xx}^{\uparrow}(\omega)$ consists of a 3-D planar layered medium (N horizontal layers) with a point source and receiver (see Fig. 4). The use of a 3-D model is essential to take into account spherical divergence (geometric spreading) in wave propagation. The medium of the nth layer is assumed to be homogeneous and can be characterized by a single dielectric permittivity ε_n, an electrical conductivity σ_n, a magnetic permeability $\mu_n = \mu_0$, and a thickness $h_n = 0.5\,\mathrm{cm}$. Green's function, formulated as an exact solution of the 3-D Maxwell equations for electromagnetic waves propagating in planar layered media, is derived by computing, with a recursive scheme, the transverse electric (TE) and magnetic (TM) global reflection coefficients of the planar layered medium in the spectral domain [64]. The transformation back to the spatial domain is performed by numerically evaluating a semi-infinite complex integral [65].

E. Bayesian Inversion Scheme

A coupled electromagnetic and hydrological inversion of the GPR and the radiometer data was performed to estimate the hydraulic parameters (θ_{r}, θ_{s}, α, and n) of the van Genuchten model. The saturated water content θ_{s} was used as a fixed parameter and was set to the value derived from the estimated sand porosity (see below). It is worth noting that θ_{s} can be experimentally obtained from radar or radiometer measurements when the soil surface is fully saturated. However, it was not possible to saturate the sand surface during the experiment due to technical constraints. Water table levels z_{w} were measured, and, therefore, considered as a known parameter for the inversions. The parameter space considered for the three free parameters θ_{r}, α, and n involved in the inversions was defined as $[0 \le \theta_{\mathrm{r}} \le 0.10\,\mathrm{m}^3 \cdot \mathrm{m}^{-3}; 1 \le \alpha \le 20\,\mathrm{m}^{-1}; 1.1 \le n \le 10]$.

The optimal values of the model parameters and their uncertainties were estimated using a Bayesian inversion method, as implemented in the DiffeRential Evolution Adaptive Metropolis (DREAM) algorithm. DREAM is a Markov chain Monte Carlo sampler that can be used to efficiently estimate the posterior probability distribution of the model parameters for nonlinear problems [46]. After convergence, the last 5000 samples were used to represent the posterior parameter distribution.

Under the assumption of independent and identically distributed Gaussian error residuals, the likelihood function ($\mathcal{L}$), which represents, in probabilistic sense, the overall distance between the model simulations and corresponding observations, can be simply defined as follows [66]:

$$\log(\mathcal{L}) \propto -\frac{N_{\mathrm{obs}}}{2} \log(SSR) \tag{9}$$

where N_{obs} is the number of observations. In order to solve the inverse problem, the log-likelihood [see (9)] is maximized using the global optimization algorithm DREAM. SSR, the sum of squared residuals, is defined according to the sensing method considered. For the off-ground GPR, SSR is defined as

$$SSR_{\mathrm{GPR}}(\mathbf{b}) = \left|\mathbf{G}_{\mathbf{xx}}^{\uparrow *} - \mathbf{G}_{\mathbf{xx}}^{\uparrow}\right|^{\mathrm{T}} \left|\mathbf{G}_{\mathbf{xx}}^{\uparrow *} - \mathbf{G}_{\mathbf{xx}}^{\uparrow}\right| \tag{10}$$

where $\mathbf{G}_{\mathbf{xx}}^{\uparrow *} = G_{xx}^{\uparrow *}(\omega, z_{\mathrm{w}})$ and $\mathbf{G}_{\mathbf{xx}}^{\uparrow} = G_{xx}^{\uparrow}(\omega, z_{\mathrm{w}}, \mathbf{b})$ are, respectively, the measured and modeled complex Green's functions in the frequency domain [antenna effects are removed using (8)], $\mathbf{b} = [\theta_{\mathrm{r}}, \alpha, n]$ is the parameter vector to be estimated. To further reduce the dimensionality of the inverse problem, the distance between the sand surface and the GPR

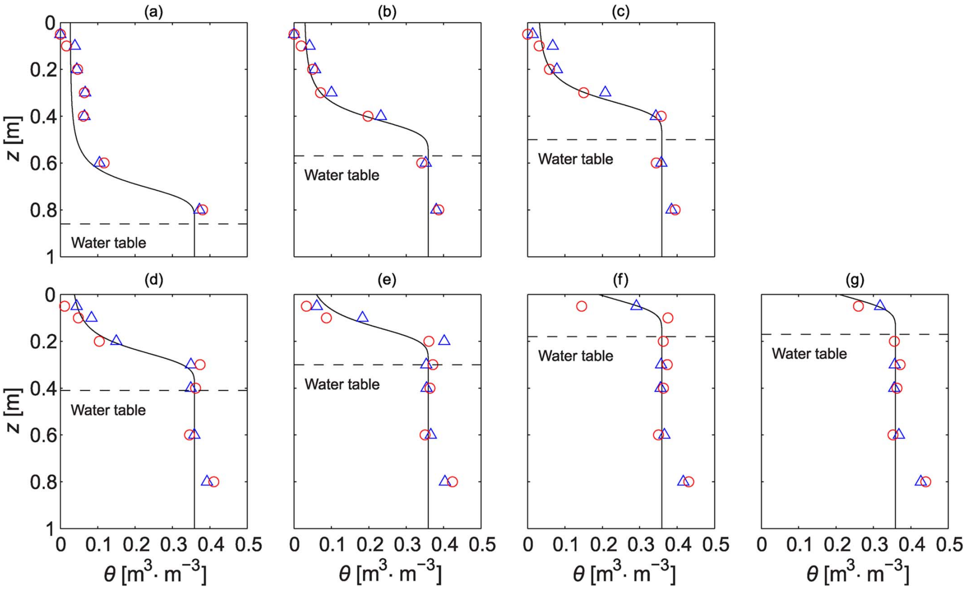

Fig. 5. Water content profiles for seven water table depths z_w. Solid lines represent the sand water retention curve estimated using all TDR data simultaneously. Markers represent TDR measurements, for the two different profiles (red circles and blue triangles). Horizontal dashed lines represent the water table levels. Note that TDR measurements at 0.80 m depth were not taken into consideration when fitting the water retention curve.

antenna phase center h_0 [m] (see Fig. 4) was previously estimated by performing inversion of the electromagnetic model in the time domain [34], [35]. The height h_0 was then used as a fixed parameter for the inversion. For the microwave radiometer (MR), SSR is defined as

$$SSR_{\mathrm{MR}}(\mathbf{b}) = \left(\mathbf{R}_\mathbf{s}^* - \mathbf{R}_\mathbf{s}\right)^\mathrm{T} \left(\mathbf{R}_\mathbf{s}^* - \mathbf{R}_\mathbf{s}\right) \tag{11}$$

where $\mathbf{R}_\mathbf{s}^* = R_\mathrm{s}^*(p, z_\mathrm{w})$ and $\mathbf{R}_\mathrm{s} = R_\mathrm{s}(p, z_\mathrm{w}, \mathbf{b})$ are, respectively, the measured and modeled reflectivities, and $\mathbf{b} = [\theta_\mathrm{r}, \alpha, n, \eta]$ is the parameter vector to be estimated. Note that the weighting factor η used in (6) was also retrieved. The sand hydraulic parameters were also estimated based on TDR-derived relative dielectric permittivities. In this case, SSR is defined as

$$SSR_{\mathrm{TDR}}(\mathbf{b}) = \left(\boldsymbol{\varepsilon}^* - \boldsymbol{\varepsilon}\right)^\mathrm{T} \left(\boldsymbol{\varepsilon}^* - \boldsymbol{\varepsilon}\right) \tag{12}$$

where $\boldsymbol{\varepsilon}^* = \varepsilon^*(z_\mathrm{TDR}, z_\mathrm{w})$ and $\boldsymbol{\varepsilon} = \varepsilon(z_\mathrm{TDR}, z_\mathrm{w}, \mathbf{b})$ are, respectively, the measured and modeled relative dielectric permittivity vectors, $\mathbf{b} = [\theta_\mathrm{s}, \theta_\mathrm{r}, \alpha, n]$ is the parameter vector to be estimated, and z_TDR is the depth of the TDR sensors. Here, θ_s was estimated and not used as a fixed parameter because several TDR sensors were also located in the saturated zone (the number of TDR sensors depended on the actual water table depth).

IV. RESULTS AND DISCUSSION

A. *In Situ TDR Data*

We considered sand water content measured with TDR at the time of radar and radiometer measurements for the inversion. However, continuous TDR measurements were taken to analyze the behavior of the *in situ* sensors and to confirm the hydrostatic equilibrium of the sand box at the times of the remote measurements. The water table levels z_w measured with a piezometer at hydrostatic equilibrium were at $z_\mathrm{w} = 0.86$ m on DOY 294, $z_\mathrm{w} = 0.57$ m on DOY 304, $z_\mathrm{w} = 0.50$ m on DOY 311, $z_\mathrm{w} = 0.41$ m on DOY 319, $z_\mathrm{w} = 0.30$ m on DOY 325, $z_\mathrm{w} = 0.18$ m on DOY 332, and $z_\mathrm{w} = 0.17$ m on DOY 343.

TDR-derived volumetric water content values θ are plotted in Fig. 5 for the seven measured water table depths z_w. Each θ data shown consists of a mean of six measurements. It should be noted that similar water content values were observed for the two measurement profiles located at the two sides of the sand box (mean standard deviation (STD) of 0.016 $\mathrm{m}^3 \cdot \mathrm{m}^{-3}$) indicating a rather homogeneous sand along the horizontal direction (see Fig. 3). The sand water retention curve was fitted to the data according to (1) and (12), whereby only a single retention curve was fitted to all TDR data without considering the data collected at a depth of 0.80 m. These water content values were omitted as they show substantially higher values compared with all other TDR readings at saturation, suggesting measurement errors.

B. *Brightness Temperatures*

Fig. 6 shows brightness temperatures (T_B^p) measured with the L-band radiometer at horizontal and vertical polarization above the experimental setup (sand box + surrounding wire grid). The radiometer measurements were performed for three different configurations, i.e., with the open sand surface $(T_{\mathrm{B,sand+grid}}^p)$, with the sand surface covered by a microwave absorber $(T_{\mathrm{B,abs+grid}}^p)$, and with the sand surface covered by a perfect reflector $(T_{\mathrm{B,ref+grid}}^p)$. Each $T_{\mathrm{B,sand+grid}}^p$ value corresponds to a mean of at least 20 measurements performed for 45 min. The STD of the repeated $T_{\mathrm{B,sand+grid}}^p$ measurements is systematically smaller than 0.3 K, which confirms the repeatability of the measurements. $T_{\mathrm{B,sand+grid}}^p$ decreases with increasing water table level z_w from 150 K to 112 K for

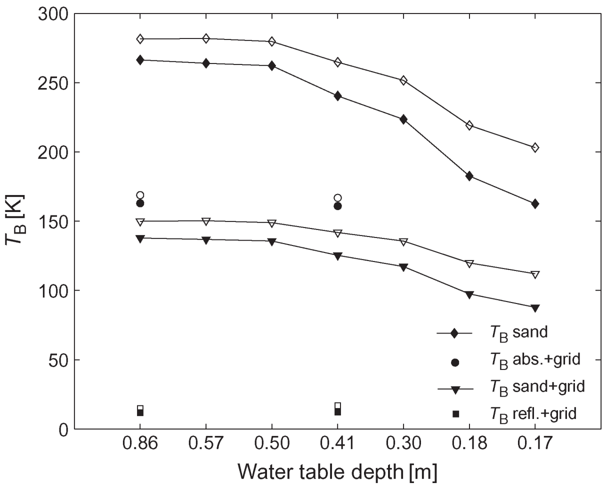

Fig. 6. Brightness temperature T_{B} measured by the L-band radiometer above the free sand surface surrounded by a wire grid (triangles) as a function of water table depth (depth scale is not linear). T_{B} measurements above the sand surface covered by an absorber (circles) and a reflector (squares) and surrounded by a wire grid are also shown for two calibration periods. Finally, T_{B} emitted from the sand only and retrieved using (6) is shown (diamonds). For all T_{B} data, horizontal and vertical polarizations are shown (filled and empty markers, respectively).

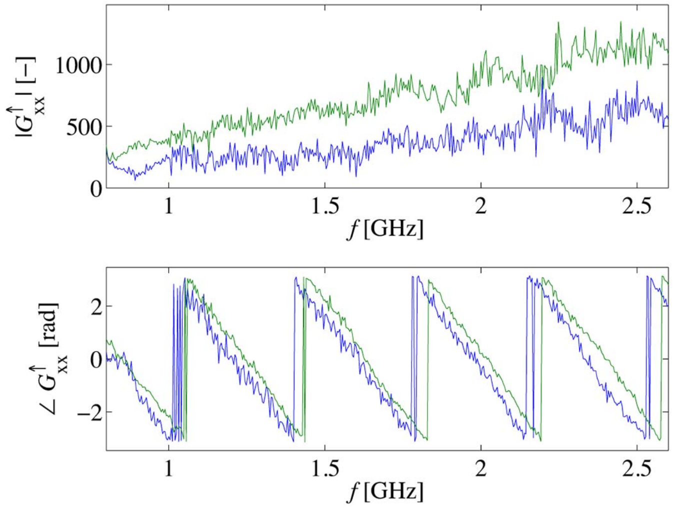

Fig. 7. Green's function in the frequency domain for measurements performed in the frequency range 0.8–2.6 GHz and for two water table depths, 0.57 (blue) and 0.17 m (green), respectively.

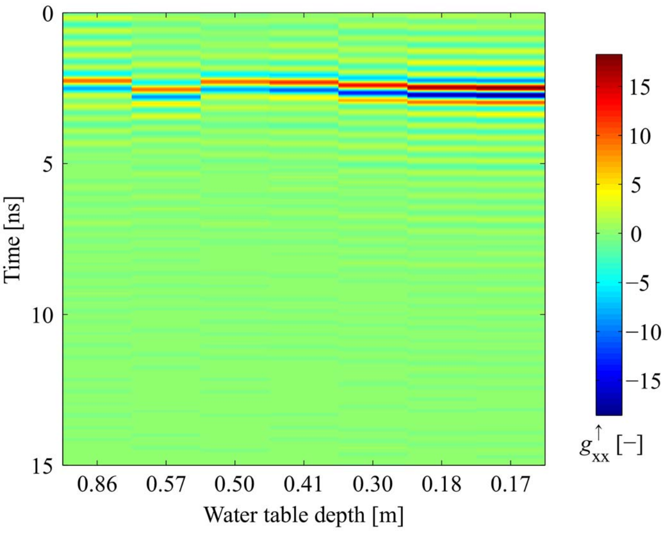

Fig. 8. Green's function in the time domain for measurements performed in the frequency range 0.8–2.6 GHz and for the seven water table depths (depth scale is not linear).

$p = \mathrm{V}$ and from 138 K to 88 K for $p = \mathrm{H}$, which results from the progressive wetting of the upper part of the sand. As expected, $T^{\mathrm{H}}_{\mathrm{B,sand+grid}}$ is systematically lower than $T^{\mathrm{V}}_{\mathrm{B,sand+grid}}$. $T^{p}_{\mathrm{B,ref+grid}}$ and $T^{p}_{\mathrm{B,abs+grid}}$ measurements were performed at the beginning and in the middle of the measurement campaign to characterize the setup. $T^{p}_{\mathrm{B,ref+grid}}$ measured above the sand box covered by a copper sheet shows low values (14.9–16.9 K for $p = \mathrm{V}$ and 11.9–12.2 K for $p = \mathrm{H}$) comparable to the sky brightness temperature (≈4.8 K). This confirms that the wire grid used as a reflector functioned properly. The remaining difference between $T^{p}_{\mathrm{B,ref+grid}}$ and T^{p}_{sky} results mainly from areas not covered by the wire grid. Additionally, $T^{p}_{\mathrm{B,ref+grid}}$ remained relatively constant for the two measurement dates, with a slight difference of 0.3 K for $p = \mathrm{H}$ and 2.0 K for $p = \mathrm{V}$. This confirms that the setup did not significantly change between the two measurements. $T^{p}_{\mathrm{B,abs+grid}}$ shows much higher brightness temperature values with 169 and 167 K for $p = \mathrm{V}$ and 163 K and 161 K for $p = \mathrm{H}$ for the first and second measurements, respectively. The similar $T^{p}_{\mathrm{B,abs+grid}}$ values observed on the two measurement dates are due to similar physical temperatures of the absorber and similar emissions from areas surrounding the sand box. The large differences between $T^{p}_{\mathrm{B,ref+grid}}$, $T^{p}_{\mathrm{B,abs+grid}}$, and $T^{p}_{\mathrm{B,sand+grid}}$ proves that our setup (see Fig. 1) is adequate to detect significant contrasts in T^{p}_{B} measured for the different configurations (reflector, absorber, and sand) and, therefore, different water content values of the sand within the box.

In addition, the radiance emitted from the sand box $T^{p}_{\mathrm{B,sand}} = (1 - R^{p}_{\mathrm{s}})\, T_{\mathrm{s}} + R^{p}_{\mathrm{s}}\, T_{\mathrm{sky}}$ was computed for each water table depth using (6) (see Fig. 6). $T^{p}_{\mathrm{B,sand}}$ values decrease with increasing water table level from 282 K to 203 K for $p = \mathrm{V}$ and from 266 to 163 K for $p = \mathrm{H}$. The difference $T^{p}_{\mathrm{B,sand}} - T^{p}_{\mathrm{B,sand+grid}}$ is greatest at the water table depth $z_{\mathrm{w}} = 0.86$ m and decreases significantly with increasing surface water content and resulting sand surface reflectivity. As expected, the polarization ratio $(T^{\mathrm{V}}_{\mathrm{B}} - T^{\mathrm{H}}_{\mathrm{B}})/(T^{\mathrm{V}}_{\mathrm{B}} + T^{\mathrm{H}}_{\mathrm{B}})$ increases with increasing sand surface water content.

C. Radar Data

Fig. 7 shows the observed radar Green's functions in the frequency domain $(G^{\uparrow}_{xx})$ for two water table depths z_{w}, and Fig. 8 shows the observed radar Green's functions in the time domain $(g^{\uparrow}_{xx})$ for the seven z_{w}. Green's function is derived from scatter functions $S_{11}(\omega)$ measured for frequencies between 0.8–2.6 GHz using (8) to filter out antenna effects. As expected, the Green's function amplitude is larger when the water table is shallower. In the time-domain counterpart, the time zero corresponds to the antenna phase center. The reflection from the sand surface is clearly visible between 2–3 ns. The surface reflection does not exactly occur at the same time

TABLE I
Estimated Hydraulic Parameters From Laboratory, TDR, Radiometer, and GPR Measurements and Their 2.5%, 50%, and 97.5% Percentile Values Obtained Using DREAM. The Lower and Upper Bounds Define the Parameter Spaces Considered for the Estimation of the Hydraulic Parameters

	θ_{s} $\mathrm{m}^3 \cdot \mathrm{m}^{-3}$	θ_{r} $\mathrm{m}^3 \cdot \mathrm{m}^{-3}$	α m^{-1}	n –
Lower bound	0.200	0.000	1.00	1.10
Upper bound	0.500	0.100	20.00	10.00
Laboratory - Best	0.374(fixed)	0.000	8.71	1.94
Laboratory - 2.5%	–	0.000	7.47	1.82
Laboratory - 50%	–	0.009	8.79	1.98
Laboratory - 97.5%	–	0.049	10.50	2.33
TDR - Best	0.359	0.026	6.21	4.59
TDR - 2.5%	0.348	0.004	5.76	3.87
TDR - 50%	0.358	0.026	6.20	4.65
TDR - 97.5%	0.367	0.049	6.68	5.73
Radiometer - Best	0.374(fixed)	0.000	5.04	3.97
Radiometer - 2.5%	–	0.000	4.01	3.29
Radiometer - 50%	–	0.008	4.98	4.18
Radiometer - 97.5%	–	0.063	5.95	5.73
GPR - Best	0.374(fixed)	0.000	6.48	4.23
GPR - 2.5%	–	0.000	6.20	3.95
GPR - 50%	–	0.000	6.48	4.25
GPR - 97.5%	–	0.002	6.83	4.62

for each measurement, as the height of the antenna was slightly different for the different measurements (0.35–0.40 m). The amplitude of the reflection increases with increasing water table level as a consequence of the increased dielectric gradient between the free-space layer and the surface-sand layer (see Fig. 4). The remaining oscillations in the time-domain signal are aliasing effects caused by the band-limited (0.8–2.6 GHz) inverse Fourier transform. No clear reflection can be observed below the surface reflection, and the water table interface is not detectable either. This means that the sand dielectric profile is rather smooth and without sharp transitions for the frequencies used and that the electromagnetic waves are almost totally attenuated in the capillary fringe and saturated zone. The assumption of a smooth dielectric profile for the unsaturated zone and an infinite lower half-space for the saturated zone in the electromagnetic model can therefore be confirmed.

D. Soil Hydraulic Parameters and Water Retention Curve

The soil moisture profiles were reconstructed from the three field measurement techniques, namely, TDR, radiometer, and off-ground GPR, and the related hydraulic parameters of the van Genuchten model [see (1)] were estimated. The reference laboratory-derived hydraulic parameters, as well as the estimated hydraulic parameters from TDR, radiometer, and GPR and their 95% corresponding confidence intervals are presented in Table I.

In the laboratory, soil hydraulic parameters are classically derived by fitting the van Genuchten model to retention data obtained from hydrostatic column experiments (see Section II-A). However, for the coarse-textured sand used in our experiment, the pores are relatively large and the air entrance value is smaller than the height of the samples used in the laboratory. Therefore, parts of the column cannot be saturated at the beginning of the laboratory experiment. Consequently, data recorded at the first pressure steps are unreliable and θ_{s} cannot be accurately estimated [3], [4]. Laboratory data at the first two pressure steps (-1 and -5 cm) were then not considered for the estimation of the hydraulic parameters. Alternatively, θ_{s} can be estimated from its porosity $\phi = \theta_{\mathrm{s}}$ expressed with

$$\phi = 1 - \rho_{\mathrm{bulk}}/\rho_{\mathrm{s}} \tag{13}$$

where ρ_{bulk} $[\mathrm{g} \cdot \mathrm{cm}^{-3}]$ is the bulk density measured from undisturbed samples ($\rho_{\mathrm{bulk}} = 1.64\,\mathrm{g} \cdot \mathrm{cm}^{-3}$) and ρ_{s} $[\mathrm{g} \cdot \mathrm{cm}^{-3}]$ is the soil particle density, which is assumed to be $\rho_{\mathrm{s}} = 2.62\,\mathrm{g} \cdot \mathrm{cm}^{-3}$ for a quartz sand. The value obtained is $\theta_{\mathrm{s}} = 0.37\,\mathrm{m}^3 \cdot \mathrm{m}^{-3}$, which is similar to the value derived from TDR data ($\theta_{\mathrm{s}} = 0.36\,\mathrm{m}^3 \cdot \mathrm{m}^{-3}$). As already mentioned, θ_{s} was not estimated from radiometer and radar measurements, as saturated conditions at the soil surface could not be attained in the sand box. Estimation of the hydraulic parameters from radiometer and radar data were therefore performed by constraining θ_{s} to the value derived from the estimated porosity [see (13)].

Table I shows that the radiometer- and GPR-derived θ_{r} values are equal to 0 such as the reference laboratory-derived θ_{r}, whereas TDR-derived θ_{r} is equal to 0.03 $\mathrm{m}^3 \cdot \mathrm{m}^{-3}$. GPR- and TDR-derived α show similar values, whereas the α estimate from radiometer is slightly smaller. In addition, the laboratory-derived α value is significantly higher compared with that derived from the three other techniques. The estimated values for n are similar when derived from the field techniques, whereas the laboratory-derived n value is significantly smaller.

In general, the confidence intervals for the estimated parameters are significantly smaller for GPR (0.002 $\mathrm{m}^3 \cdot \mathrm{m}^{-3}$ for θ_{r}, 0.63 m^{-1} for α, and 0.67 for n) compared with TDR (0.045 $\mathrm{m}^3 \cdot \mathrm{m}^{-3}$ for θ_{r}, 0.92 m^{-1} for α, and 1.86 for n), radiometer (0.063 $\mathrm{m}^3 \cdot \mathrm{m}^{-3}$ for θ_{r}, 1.94 m^{-1} for α, and 2.44 for n), and the laboratory measurements (0.049 $\mathrm{m}^3 \cdot \mathrm{m}^{-3}$ for θ_{r}, 3.03 m^{-1} for α, and 0.52 for n), except for the confidence interval for n, which is slightly smaller for the laboratory measurements. The smaller confidence intervals of the GPR-derived parameters could be explained by the larger amount of information contained in the GPR data (226 frequencies) compared with the TDR (2 × 7 positions) and the radiometer data (2 polarizations). In addition, the lower frequencies of the GPR provide information for greater depths compared with the radiometer. It is worth noting that the high accuracy of the GPR electromagnetic model for the configuration used (e.g., homogeneous sand box, smooth soil surface, no vegetation cover) could also lead to relatively small confidence intervals for the estimates.

Parameter η, which is the fractional amount of the measured radiance emitted from the sand box, was also estimated from radiometer data simultaneously with the hydraulic parameters. The estimated value of η is 0.50 with a 95% confidence interval of [0.49 0.54]. This value is similar to that obtained from the antenna characterization ($\eta = 0.48$) and the absorber and reflector measurements ($\eta = 0.54$).

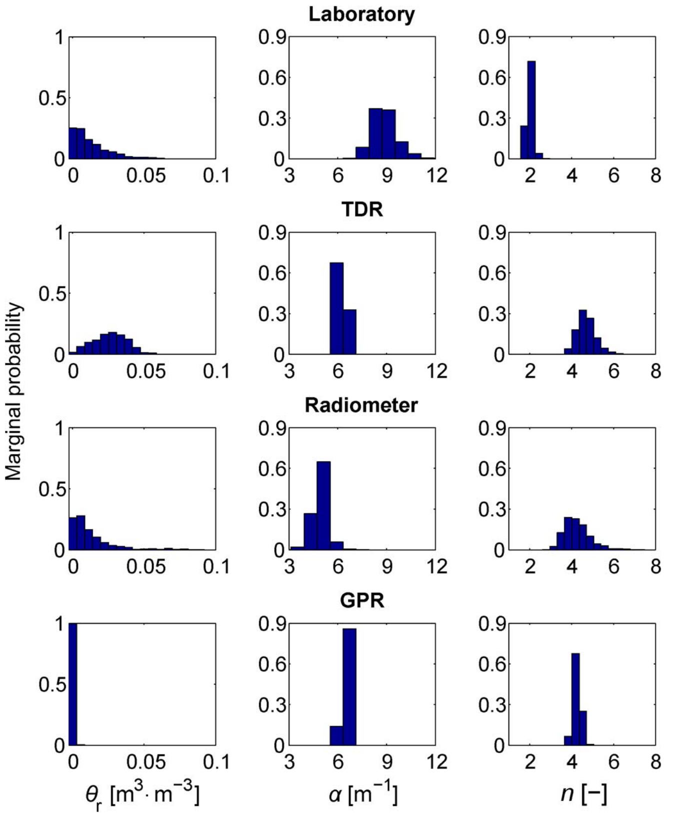

Fig. 9. Marginal posterior probability distribution of the model parameters estimated by the different methods (laboratory, TDR sensors, radiometer, and GPR). Parameter distributions are obtained using the last 5000 samples generated with DREAM.

TABLE II
CORRELATIONS BETWEEN THE ESTIMATED HYDRAULIC PARAMETERS FROM TDR, RADIOMETER, AND GPR MEASUREMENTS

	α vs n	α vs θ_r	n vs θ_r
TDR	0.08	0.55	0.54
Radiometer	-0.42	-0.37	0.46
GPR	-0.73	0.05	0.15

To gain more information about the parameter uncertainties, the marginal posterior distribution of the model parameters estimated by the different techniques is plotted in Fig. 9. The parameter distributions are obtained using the last 5000 samples generated with DREAM. As can be seen, very narrow confidence intervals are obtained for the GPR-derived parameters $(\theta_r, \alpha, \text{and } n)$ and n derived in the laboratory.

Table II shows the correlation between the hydraulic parameters for the three measurement techniques applied to the sand box. The correlation between α and n is large for the GPR inversion, whereby a general correlation between these two parameters has already been detected in various publications [5], [67]–[69]. Hardly any correlation between these two parameters can be found using TDR data. The correlation is intermediate for the radiometer-derived parameters. This can also be clearly observed in Fig. 10, which shows

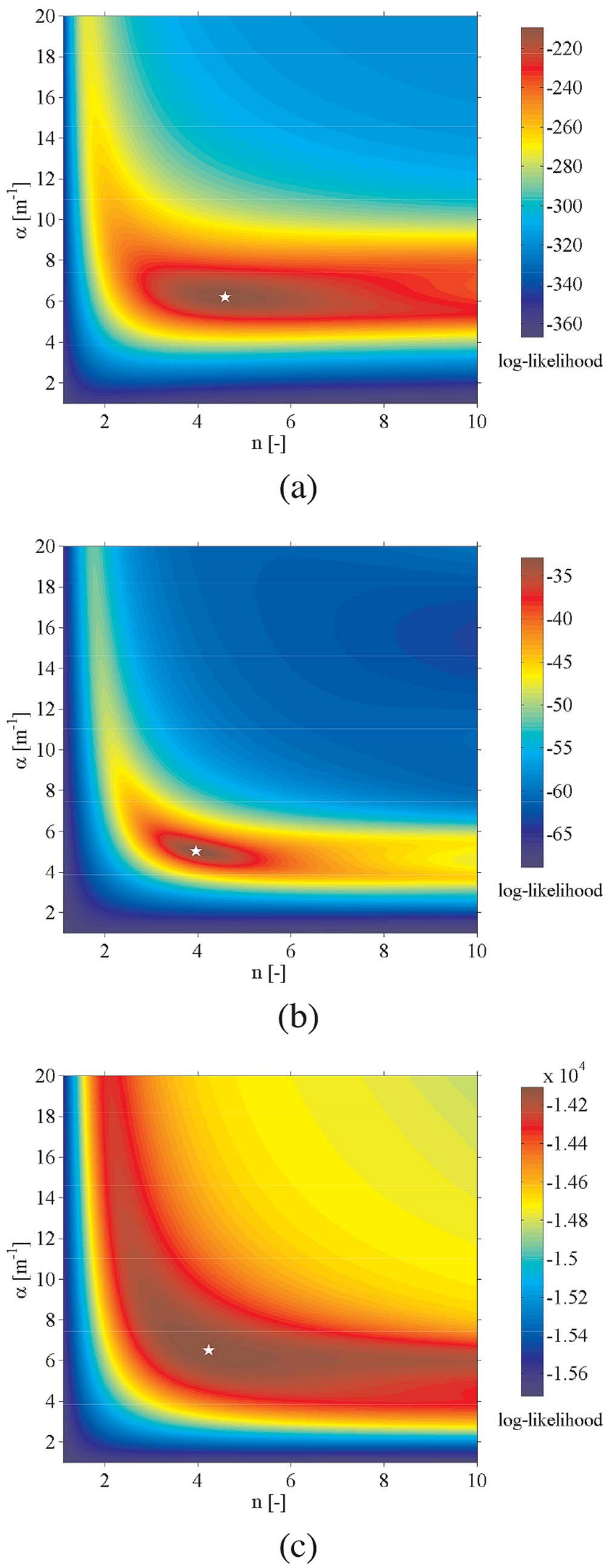

(a)

(b)

(c)

Fig. 10. Response surfaces of the log-likelihood [see (9)] in the α–n parameter plane for the TDR (a), radiometer (b), and GPR (c) inversions. The asterisk represents the global maximum. Note that the color scale differs for the three response surfaces.

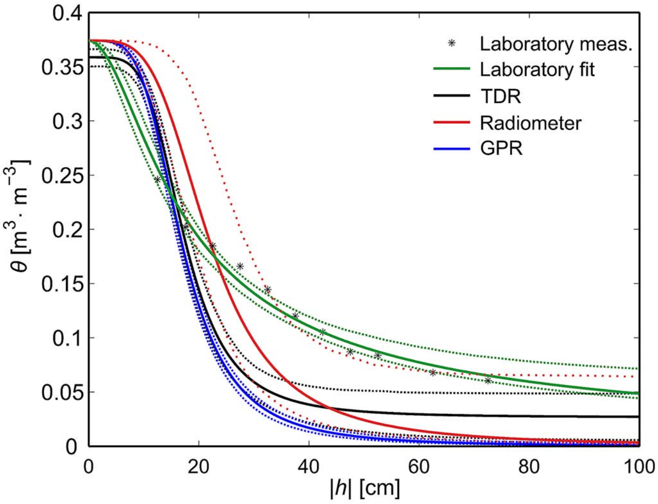

Fig. 11. Water retention curves (solid lines) and their associated 95% confidence intervals (dotted lines) based on the van Genuchten parametrization and estimated by the different methods (laboratory, TDR sensors, radiometer, and GPR). Laboratory data obtained using the sand bed method are also shown (black asterisks).

the response surfaces of the log-likelihood [see (9)] in the α–n parameter plane for each sensing technique. For GPR, the global maximum region exhibits a banana shape, which suggests an important negative correlation between the parameters [see Fig. 10(c)], whereas for TDR, the response surface shows an elliptical global maximum region parallel to the n axis [see Fig. 10(a)]. As noted before (see Table II), the correlation is intermediate for the radiometer [see Fig. 10(b)]. For each response surface, no local maxima can be observed in addition to the global maximum. Table II also shows the correlation between α and θ_r, as well as between n and θ_r for the three sensing techniques. These correlations are fairly high for the TDR and radiometer, and lower for the GPR. In addition, a negative correlation between α and θ_r can be observed for the radiometer technique.

Finally, Fig. 11 compares the sand water retention curves computed using the van Genuchten hydraulic parameter estimates and their 95% confidence intervals retrieved by the laboratory and field techniques. As shown, GPR- and radiometer-derived water retention curves are in close agreement with the TDR-derived water retention curve. The main difference is observed in the dry range, where the radiometer and GPR-derived estimates of the sand water content approach a residual water content, θ_r, close to 0, whereas the residual water content for TDR is slightly higher. On the other hand, the retention curve fitted on the laboratory data diverges substantially from the other retention curves.

V. SUMMARY AND CONCLUSION

We have investigated the feasibility of estimating key soil hydraulic properties from 1.4 GHz radiometer and 0.8–2.6 GHz GPR data. In particular, measurements were taken above an outdoor sand box subjected to a series of vertical water content profiles in hydrostatic equilibrium with a water table located at different depths. Radiometer data were described using a coherent RT model, whereas GPR data were modeled using full-wave layered medium Green's functions and an intrinsic antenna representation. These forward models were inverted to reconstruct the water content profiles, and thereby to estimate the sand water retention curve described using the van Genuchten model. Uncertainty of the estimated hydraulic parameters was quantified using the Bayesian-based DREAM algorithm. The results of the inversions show that the radar and radiometer data contain sufficient information to estimate the sand water retention curve and its related hydraulic parameters with relatively good accuracy compared with TDR data. Additionally, parameter uncertainties for the radiometer are in the range of the uncertainties of the TDR-derived parameters, whereby the GPR-based estimates showed a much lower uncertainty compared with all other techniques, which can be explained by the large amount of information content available in the GPR data and the lower frequencies used. The results were compared with reference laboratory measurements to obtain an independent set of hydraulic parameters for the sand, but these data showed a bias with respect to the field techniques.

This study provides valuable insights into the information content in passive and active microwave data with respect to continuously varying soil moisture profiles and corresponding soil hydraulic properties. The main benefit of a knowledge of soil hydraulic properties for remote sensing applications is their use in soil hydrodynamic models for predicting soil moisture deeper than the remote sensing sensitivity depth (a few centimeters) and with a better time resolution than remote sensor acquisitions. It is also important for quantifying water and energy fluxes between the soil and the atmosphere.

Although, relatively good results were obtained in this study, and improvements are still possible through a better quantification of the different sources of uncertainties in this Bayesian framework, a major challenge for remote sensing applications is to cope with the inherent variability of soil hydraulic properties within the sensor footprints, with respect to depth, and to some extent, with respect to time (agricultural fields). In addition, complications such as soil roughness and vegetation cover significantly reduce the accuracy with which state variables such as soil moisture can actually be retrieved.

Future research will focus on transient conditions to further estimate hydraulic conductivity parameters. In addition, the experimental setup is of particular interest for further study of the impact of, for example, organic soil layers, soil surface roughness, and vegetation on radiometer and radar measurements.

ACKNOWLEDGMENT

The authors would like to thank X. Li of the Beijing Normal University, F. Laurent of the Université catholique de Louvain, and A. Langen and S. Pickel of Forschungszentrum Jülich for their technical assistance. The authors also thank J. A. Huisman of Forschungszentrum Jülich for constructive discussions and J. A. Vrugt of the University of California for providing the DREAM code.

REFERENCES

[1] A. K. Betts, J. H. Ball, A. C. M. Beljaars, M. J. Miller, and P. A. Viterbo, "The land surface-atmosphere interaction: A review based on observational and global modeling perspectives," *J. Geophys. Res., Atmos.*, vol. 101, no. D3, pp. 7209–7225, Mar. 1996.

[2] R. D. Koster *et al.*, "Regions of strong coupling between soil moisture and precipitation," *Science*, vol. 305, no. 5687, pp. 1138–1140, Aug. 2004.

[3] A. Peters and W. Durner, "Improved estimation of soil water retention characteristics from hydrostatic column experiments," *Water Resour. Res.*, vol. 42, no. 11, Nov. 2006, Art. ID. W11401.

[4] M. Bittelli and M. Flury, "Errors in water retention curves determined with pressure plates," *Soil Sci. Soc. Amer. J.*, vol. 73, no. 5, pp. 1453–1460, Sep. 2009.

[5] C. M. Mboh, J. A. Huisman, and H. Vereecken, "Feasibility of sequential and coupled inversion of time domain reflectometry data to infer soil hydraulic parameters under falling head infiltration," *Soil Sci. Soc. Amer. J.*, vol. 75, no. 3, pp. 775–786, May 2011.

[6] D. L. Corwin, J. Hopmans, and G. H. de Rooij, "From field- to landscape-scale vadose zone processes: Scale issues, modeling, and monitoring," *Vadose Zone J.*, vol. 5, no. 1, pp. 129–139, Jan. 2006.

[7] H. Vereecken, R. Kasteel, J. Vanderborght and T. Harter, "Upscaling hydraulic properties and soil water flow processes in heterogeneous soils: A review," *Vadose Zone J.*, vol. 6, no. 1, pp. 1–28, Feb. 2007.

[8] J. H. M. Wösten, Y. A. Pachepsky, and W. J. Rawls, "Pedotransfer functions: Bridging gap between available basic soil data and missing soil hydraulic characteristics," *J. Hydrol.*, vol. 251, no. 3/4, pp. 123–150, 2001.

[9] H. Vereecken *et al.*, "Using pedotransfer functions to estimate the van Genuchten-Mualem soil hydraulic properties: A review," *Vadose Zone J.*, vol. 9, no. 4, pp. 795–820, Nov. 2010.

[10] M. G. Schaap, "Accuracy and uncertainty in PTF predictions" in *Development of Pedotransfer Functions in Soil Hydrology*, vol. 30, Y. P. Rawls and W. J., Eds. Amsterdam, The Netherlands: Elsevier, 2004, pp. 33–43.

[11] H. L. Deng, M. Ye, M. G. Schaap, and R. Khaleel, "Quantification of uncertainty in pedotransfer function-based parameter estimation for unsaturated flow modeling," *Water Resour. Res.*, vol. 45, no. 4, Apr. 2009, Art. ID. W04409.

[12] F. T. Ulaby, M. K. Moore, and A. K. Fung, *Microwave Remote Sensing: Active and Passive*, vol. I, *Fundamentals and Radiometry*. Reading, MA, USA: Addison-Wesley, 1981.

[13] F. T. Ulaby, M. K. Moore, and A. K. Fung, *Microwave Remote Sensing: Active and Passive*, vol. II, *Radar Remote Sensing and Surface Scattering and Emission Theory*. Norwood, MA, USA: Artech House, 1982.

[14] F. T. Ulaby, M. K. Moore, and A. K. Fung, *Microwave Remote Sensing: Active and Passive*, vol. III, *From Theory to Applications*. Norwood, MA, USA: Artech House, 1986.

[15] T. J. Schmugge, W. P. Kustas, J. C. Ritchie, T. J. Jackson, and A. Rango, "Remote sensing in hydrology," *Adv. Water Resourc.*, vol. 25, no. 8–12, pp. 1367–1385, Aug. 2002.

[16] C. Mätzler, *Thermal Microwave Radiation: Applications for Remote Sensing*. London, U.K.: The Inst. Eng. Technol., 2006, ser. IET Electromagnetic Waves series 52.

[17] W. Wagner *et al.*, "Operational readiness of microwave remote sensing of soil moisture for hydrologic applications," *Nordic Hydrol.*, vol. 38, no. 1, pp. 1–20, 2007.

[18] J. C. Shi *et al.*, "Progresses on microwave remote sensing of land surface parameters," *Sci. China–Earth Sci.*, vol. 55, no. 7, pp. 1052–1078, Jul. 2012.

[19] H. Vereecken, L. Weihermüller, F. Jonard, and C. Montzka, "Characterization of crop canopies and water stress related phenomena using microwave remote sensing methods: A review," *Vadose Zone J.*, vol. 11, no. 2, May 2012.

[20] Y. H. Kerr *et al.*, "Soil moisture retrieval from space: The Soil Moisture and Ocean Salinity (SMOS) mission," *IEEE Trans. Geosci. Remote Sens.*, vol. 39, no. 8, pp. 1729–1735, Aug. 2001.

[21] Y. H. Kerr *et al.*, "The SMOS mission: New tool for monitoring key elements of the global water cycle," *Proc. IEEE*, vol. 98, no. 5, pp. 666–687, May 2010.

[22] S. Mecklenburg *et al.*, "ESA's soil moisture and ocean salinity mission: Mission performance and operations," *IEEE Trans. Geosci. Remote Sens.*, vol. 50, no. 5, pp. 1354–1366, May 2012.

[23] D. Entekhabi *et al.*, "The Soil Moisture Active Passive (SMAP) mission," *Proc. IEEE*, vol. 98, no. 5, pp. 704–716, May 2010.

[24] N. N. Das, D. Entekhabi, and E. G. Njoku, "An algorithm for merging SMAP radiometer and radar data for high-resolution soil-moisture retrieval," *IEEE Trans. Geosci. Remote Sens.*, vol. 49, no. 5, pp. 1504–1512, May 2011.

[25] P. J. Camillo, P. E. Oneill, and R. J. Gurney, "Estimating soil hydraulic parameters using passive microwave data," *IEEE Trans. Geosci. Remote Sens.*, vol. GE-24, no. 6, pp. 930–936, Nov. 1986.

[26] E. J. Burke, R. J. Gurney, L. P. Simmonds, and P. E. O'Neill, "Using a modeling approach to predict soil hydraulic properties from passive microwave measurements," *IEEE Trans. Geosci. Remote Sens.*, vol. 36, no. 2, pp. 454–462, Mar. 1998.

[27] N. M. Mattikalli, E. T. Engman, T. J. Jackson, and L. R. Ahuja, "Microwave remote sensing of temporal variations of brightness temperature and near-surface soil water content during a watershed-scale field experiment, and its application to the estimation of soil physical properties," *Water Resour. Res.*, vol. 34, no. 9, pp. 2289–2299, Sep. 1998.

[28] D. H. Chang and S. Islam, "Estimation of soil physical properties using remote sensing and artificial neural network," *Remote Sens. Environ.*, vol. 74, no. 3, pp. 534–544, Dec. 2000.

[29] J. A. Santanello *et al.*, "Using remotely sensed estimates of soil moisture to infer soil texture and hydraulic properties across a semi-arid watershed," *Remote Sens. Environ.*, vol. 110, no. 1, pp. 79–97, Sep. 2007.

[30] K. W. Harrison, S. V. Kumar, C. D. Peters-Lidard, and J. A. Santanello, "Quantifying the change in soil moisture modeling uncertainty from remote sensing observations using Bayesian inference techniques," *Water Resour. Res.*, vol. 48, no. 11, Nov. 2012, Art. ID. W11514.

[31] A. V. M. Ines and B. P. Mohanty, "Near-surface soil moisture assimilation for quantifying effective soil hydraulic properties using genetic algorithms: 2. Using airborne remote sensing during SGP97 and SMEX02," *Water Resour. Res.*, vol. 45, no. 1, Jan. 2009, Art. ID. W01408.

[32] C. Montzka *et al.*, "Hydraulic parameter estimation by remotely sensed top soil moisture observations with the particle filter," *J. Hydrol.*, vol. 399, no. 2011, pp. 410–421, Mar. 2011.

[33] B. P. Mohanty, "Soil hydraulic property estimation using remote sensing: A review," *Vadose Zone J.*, vol. 12, no. 4, pp. 1–9, 2013.

[34] S. Lambot *et al.*, "Analysis of air-launched ground-penetrating radar techniques to measure the soil surface water content," *Water Resour. Res.*, vol. 42, no. 11, Nov. 2006, Art. ID. W11403.

[35] F. Jonard *et al.*, "Mapping field-scale soil moisture with L-band radiometer and ground-penetrating radar over bare soil," *IEEE Trans. Geosci. Remote Sens.*, vol. 49, no. 8, pp. 2863–2875, Aug. 2011.

[36] J. Minet, P. Bogaert, M. Vanclooster, and S. Lambot, "Validation of ground penetrating radar full-waveform inversion for field scale soil moisture mapping," *J. Hydrol.*, vol. 424–425, pp. 112–123, Mar. 2012.

[37] S. Lambot, E. C. Slob, I. van den Bosch, B. Stockbroeckx, and M. Vanclooster, "Modeling of ground-penetrating radar for accurate characterization of subsurface electric properties," *IEEE Trans. Geosci. Remote Sens.*, vol. 42, no. 11, pp. 2555–2568, Nov. 2004.

[38] A. Klotzsche *et al.*, "Full-waveform inversion of cross-hole ground-penetrating radar data to characterize a gravel aquifer close to the Thur River, Switzerland," *Near Surf. Geophys.*, vol. 8, no. 6, pp. 635–649, 2010.

[39] S. Lambot and F. André, "Full-wave modeling of near-field radar data for planar layered media reconstruction," *IEEE Trans. Geosci. Remote Sens.*, vol. 52, no. 5, pp. 2295–2303, May 2014.

[40] A. Binley, G. Cassiani, R. Middleton, and P. Winship, "Vadose zone flow model parameterisation using cross-borehole radar and resistivity imaging," *J. Hydrol.*, vol. 267, no. 3/4, pp. 147–159, Oct. 2002.

[41] D. F. Rucker and T. P. A. Ferré, "Parameter estimation for soil hydraulic properties using zero-offset borehole radar: Analytical method," *Soil Sci. Soc. Amer. J.*, vol. 68, no. 5, pp. 1560–1567, Sep. 2004.

[42] M. B. Kowalsky *et al.*, "Estimation of field-scale soil hydraulic and dielectric parameters through joint inversion of GPR and hydrological data," *Water Resour. Res.*, vol. 41, no. 11, Nov. 2005, Art. ID. W11425.

[43] M. Looms, A. Binley, K. H. Jensen, L. Nielsen, and T. M. Hansen, "Identifying unsaturated hydraulic parameters using an integrated data fusion approach on cross-borehole geophysical data," *Vadose Zone J.*, vol. 7, no. 1, pp. 238–248, Feb. 2008.

[44] S. Lambot *et al.*, "Remote estimation of the hydraulic properties of a sand using full-waveform integrated hydrogeophysical inversion of time-lapse, off-ground GPR data," *Vadose Zone J.*, vol. 8, no. 3, pp. 743–754, Aug. 2009.

[45] K. Z. Jadoon *et al.*, "Estimation of soil hydraulic parameters in the field by integrated hydrogeophysical inversion of time-lapse ground-penetrating radar data," *Vadose Zone J.*, vol. 11, no. 4, Nov. 2012.

[46] J. A. Vrugt *et al.*, "Accelerating Markov Chain Monte Carlo simulation by differential evolution with self-adaptive randomized subspace

sampling," *Int. J. Nonlinear Sci. Numer. Simul.*, vol. 10, no. 3, pp. 273–290, Mar. 2009.

[47] T. J. Heimovaara and W. Bouten, "A computer-controlled 36-channel time domain reflectometry system for monitoring soil-water contents," *Water Resour. Res.*, vol. 26, no. 10, pp. 2311–2316, Oct. 1990.

[48] M. Schwank *et al.*, "ELBARA II, an L-band radiometer system for soil moisture research," *Sensors*, vol. 10, no. 1, pp. 584–612, Jan. 2010.

[49] M. Schwank *et al.*, "L-band radiative properties of vine vegetation at the MELBEX III SMOS cal/val site," *IEEE Trans. Geosci. Remote Sens.*, vol. 50, no. 5, pp. 1587–1601, May 2012.

[50] F. Jonard *et al.*, "Characterization of tillage effects on the spatial variation of soil properties using ground-penetrating radar and electromagnetic induction," *Geoderma*, vol. 207/208, pp. 310–322, Oct. 2013.

[51] M. T. van Genuchten, "A closed-form equation for predicting the hydraulic conductivity of unsaturated soils," *Soil Sci. Soc. Amer. J.*, vol. 44, pp. 892–898, Sep. 1980.

[52] G. Topp, J. L. Davis, and A. P. Annan, "Electromagnetic determination of soil water content: Measurements in coaxial transmission lines," *Water Resour. Res.*, vol. 16, no. 3, pp. 574–582, Jun. 1980.

[53] O. H. Jacobsen and P. Schjonning, "A laboratory calibration of time-domain reflectometry for soil-water measurement including effects of bulk-density and texture," *J. Hydrol.*, vol. 151, no. 2–4, pp. 147–157, Nov. 1993.

[54] D. A. Robinson, S. B. Jones, J. M. Wraith, D. Or, and S. P. Friedman, "A review of advances in dielectric and electrical conductivity measurement in soils using time-domain reflectometry," *Vadose Zone J.*, vol. 2, no. 4, pp. 444–475, Nov. 2003.

[55] K. Roth, R. Schulin, H. Flühler, and W. Attinger, "Calibration of time-domain reflectometry for water-content measurement using a composite dielectric approach," *Water Resour. Res.*, vol. 26, no. 10, pp. 2267–2273, Oct. 1990.

[56] T. J. Heimovaara, W. Bouten, and J. M. Verstraten, "Frequency domain analysis of time domain reflectometry waveforms, 2, a four-component complex dielectric mixing model for soils," *Water Resour. Res.*, vol. 30, no. 2, pp. 201–209, Feb. 1994.

[57] P. Debye, *Polar Molecules*. New York, NY, USA: Reinhold, 1929.

[58] J. A. Lane and J. A. Saxton, "Dielectric dispersion in pure polar liquids at very high radio frequencies. III. The effect of electrolytes in solution," *Proc. R. Soc. Lond. A, Math. Phys. Sci.*, vol. 214, no. 1119, pp. 531–545, Oct. 1952.

[59] L. A. Klein and C. T. Swift, "An improved model for the dielectric constant of sea water at microwave frequencies," *IEEE Trans. Antennas Propag.*, vol. AP-25, no. 1, pp. 104–111, Jan. 1977.

[60] A. Stogryn, "Equations for calculating the dielectric constant of saline water," *IEEE Trans. Microw. Theory Tech.*, vol. MTT-19, no. 8, pp. 733–736, Aug. 1971.

[61] T. Pellarin *et al.*, "Two-year global simulation of L-band brightness temperatures over land," *IEEE Trans. Geosci. Remote Sens.*, vol. 41, no. 9, pp. 2135–2139, Sep. 2003.

[62] J. A. Dobrowolski, "Optical properties of films and coatings" in *Handbook of Optics*, vol. I, M. Bass, E. W. Van Stryland, D. R. Williams, and W. L. Wolfe, Eds. New York, NY, USA: McGraw-Hill, 1995, pp. 42.

[63] S. Lambot, J. Rhebergen, I. van den Bosch, E. C. Slob, and M. Vanclooster, "Measuring the soil water content profile of a sandy soil with an off-ground monostatic ground penetrating radar," *Vadose Zone J.*, vol. 3, no. 4, pp. 1063–1071, Nov. 2004.

[64] E. C. Slob and J. Fokkema, "Coupling effects of two electric dipoles on an interface," *Radio Sci.*, vol. 37, no. 5, pp. 1073, 2002.

[65] S. Lambot, E. Slob, and H. Vereecken, "Fast evaluation of zero-offset Green's function for layered media with application to ground-penetrating radar," *Geophys. Res. Lett.*, vol. 34, no. 21, Nov. 2007, Art. ID. L21405.

[66] B. Scharnagl, J. A. Vrugt, H. Vereecken, and M. Herbst, "Inverse modelling of in situ soil water dynamics: Investigating the effect of different prior distributions of the soil hydraulic parameters," *Hydrol. Earth Syst. Sci.*, vol. 15, no. 10, pp. 3043–3059, 2011.

[67] J. A. Vrugt, W. Bouten, and A. H. Weerts, "Information content of data for identifying soil hydraulic parameters from outflow experiments," *Soil Sci. Soc. Amer. J.*, vol. 65, no. 1, pp. 19–27, Jan. 2001.

[68] S. Lambot, M. Javaux, F. Hupet, and M. Vanclooster, "A global multilevel coordinate search procedure for estimating the unsaturated soil hydraulic properties," *Water Resour. Res.*, vol. 38, no. 11, pp. 6:1–6:15, Nov. 2002.

[69] N. K. C. Twarakavi, H. Saito, J. Simunek, and M. T. van Genuchten, "A new approach to estimate soil hydraulic parameters using only soil water retention data," *Soil Sci. Soc. Amer. J.*, vol. 72, no. 2, pp. 471–479, Mar. 2008.

François Jonard received the M.Sc. and Ph.D. degrees in environmental engineering from the Université catholique de Louvain (UCL), Louvain-la-Neuve, Belgium, in 2002 and 2012, respectively.

From 2003 to 2004, he worked with UCL as a Research Assistant on modeling water fluxes in forest ecosystems. From 2006 to 2009, he was a Consultant with the European Commission in the fields of geographic information systems and remote sensing of the environment. Since 2009, he has been with the Agrosphere, Institute of Bio- and Geosciences, Forschungszentrum Jülich, Jülich, Germany. In 2011, he spent several months at the NASA Goddard Space Flight Center, Greenbelt, MD, as a Visiting Scientist, working in the context of the Soil Moisture Active Passive mission. His current research interests include hydrogeophysics and microwave remote sensing of soil and vegetation.

Lutz Weihermüller received the Diploma degree in geography from the Universität Bremen, Bremen, Germany and the Ph.D. degree in the field of numerical modeling from the Universität Bonn, Bonn, Germany, in 2005.

He is currently working as a Postdoctoral Researcher with the Forschungszentrum Jülich, Jülich, Germany. His research interests are the numerical modeling of water, solute, and gas transport in the unsaturated zone and parameter estimation for various applications. Additionally, he works on different hydrogeophysical methods such as ground-penetrating radar and radiometry for soil water monitoring.

Dr. Weihermüller is a member of the American Geophysical Union, European Geosciences Union, and Soil Science Society of America.

Mike Schwank received the bachelor's degree in electrical engineering in 1989 and the Ph.D. degree in physics from ETH-Zürich, Zürich, Switzerland, in 1999.

From 1999–2003, he has experience with industrial research and development (R&D) in the fields of micro-optics and telecommunications. From 2007–2009 and since 2013, he has part-time employments at GAMMA Remote Sensing AG, Gümligen, Switzerland and at the Swiss Federal Institute for Forest, Snow and Landscape Research (WSL), Birmensdorf, Switzerland. He is experienced with leading Ph.D. students, and the coordination of large research projects such as TERENO (Terrestrial Environmental Observatories). The main focus of his research since 2003 is on microwave remote sensing studies in support of the Soil Moisture and Ocean Salinity mission.

Khan Zaib Jadoon received the Ph.D. degree in environmental engineering from the Université catholique de Louvain, Louvain-la-Neuve, Belgium, in 2010.

From 2007 to 2011, he was with the Agrosphere, Institute of Bio- and Geosciences, Forschungszentrum Jülich, Germany, as a Research Assistant and Postdoctoral Researcher. In early 2012, he joined King Abdullah University of Science and Technology (KAUST), Thuwal, Saudi Arabia, as a Postdoctoral Researcher and presently working with Earth System Observation and Modeling group at KAUST as a Research Scientist.

Dr. Jadoon is a member of the American Geophysical Union, European Geosciences Union, Society of Exploration Geophysicists, and Environmental and Engineering Geophysical Society.

Harry Vereecken received the M.Sc. degree in agricultural engineering and the Ph.D. degree in agricultural sciences from the Katholieke Universiteit Leuven, Leuven, Belgium, in 1982 and 1988, respectively. His Ph.D. degree was on the development of pedotransfer functions to estimate soil hydraulic properties.

From 1988 to 1990, he was a Research Assistant on modeling nitrogen and water fluxes in soils and groundwater. From 1990 until 1992, he worked as a Researcher with the Institute of Petroleum and Organic Geochemistry, Forschungszentrum Jülich, Jülich Germany, and he became Head of division "Behavior of pollutants in geological systems" at the same institute from 1992 to 2000. He was appointed Director of the Institute Agrosphere in 2000. His current field of research is modeling of flow and transport processes in soils and hydrogeophysics.

Sébastien Lambot received the M.Sc. and Ph.D. degrees in agricultural and environmental engineering from the Université catholique de Louvain (UCL), Louvain-La-Neuve, Belgium, in 1999 and 2003, respectively.

From 2004 to 2005, he was with the Delft University of Technology, Delft, The Netherlands, as a European Marie-Curie Postdoctoral Scientist. From 2006 to 2012, he was with Forschungszentrum Jülich, Jülich, Germany, as a Research Group Leader. Since 2006, he has been a Professor and Fonds de la Recherche Scientifique (FNRS) Researcher with UCL. His current research interests include ground-penetrating radar and electromagnetic induction forward and inverse modeling for digital soil mapping and nondestructive testing of materials.

Dr. Lambot was the General Chair of the Third International Workshop on Advanced Ground Penetrating Radar in 2005 and the General Chair of the 15th International Conference on Ground Penetrating Radar in 2014. He is an Associate Editor for the *Vadose Zone Journal*.